Estimating Fiber Orientation Distribution through Blockwise Adaptive Thresholding with Application to HCP Young Adults Data

Seungyong Hwang*, Thomas C. M. Lee, Debashis Paul, Jie Peng[†] University of California, Davis

Abstract

Due to recent technological advances, large brain imaging data sets can now be collected. Such data are highly complex so extraction of meaningful information from them remains challenging. Thus, there is an urgent need for statistical procedures that are computationally scalable and can provide accurate estimates that capture the neuronal structures and their functionalities. We propose a fast method for estimating the fiber orientation distribution(FOD) based on diffusion MRI data. This method models the observed dMRI signal at any voxel as a convolved and noisy version of the underlying FOD, and utilizes the spherical harmonics basis for representing the FOD, where the spherical harmonic coefficients are adaptively and nonlinearly shrunk by using a James-Stein type estimator. To further improve the estimation accuracy by enhancing the localized peaks of the FOD, as a second step a super-resolution sharpening process is then applied. The resulting estimated FODs can be fed to a fiber tracking algorithm to reconstruct the white matter fiber tracts. We illustrate the overall methodology using both synthetic data and data from the Human Connectome Project.

* Codes and example scripts for simulation and HCP data application can be found at https://github.com/vic-dragon/BJS.

Keywords: James-Stein estimator, dMRI, Neuroimaging, HCP, Nonparametric regression

^{*}The authors gratefully acknowledge the following support: DMS-1512945, DMS-1513484, DMS-1713120, DMS-1811405, DMS-1811661, DMS-1916125, NIH 1R01EB021707.

[†]Correspondence author: jiepeng@ucdavis.edu

1 Introduction

Diffusion-weighted magnetic resonance imaging (D-MRI) (Le Bihan et al., 2001; Mori, 2007) has become a widely used, non-invasive tool for characterizing tissue microstructure in vivo through measuring the diffusion of water molecules. In D-MRI experiments, multiple pulsed magnetic gradient fields are successively applied to the tissue sample, so that the measured signal intensity is sensitized with the amount of water diffusion along the respective gradient directions. Since water diffusion is faster along tissue structures such as neuronal fiber bundles, water diffusion can be used as a proxy to probe architecture of biological tissues. D-MRI has many applications including in white matter fiber tracks reconstruction and in studying neurodegenerative diseases such as the Alzheimer's.

D-MRI data consist of diffusion weighted signal measurements on a 3D spatial grid (of the sample) along a set of predetermined gradient directions (Bammer et al., 2009; Beaulieu, 2002; Chanraud et al., 2010; Mukherjee et al., 2008). For example, a typical data set from the Human Connectome Project (HCP) has diffusion measurements along 270 (90 for each of the three shells of b=1000, 2000, and 3000 s/mm^2) gradient directions at each voxel on a $145 \times 174 \times 145$ 3D grid of the brain with side length of each voxel being 1.25mm. After preprocessing (including registration and isolation of the brain, eddy current correction, etc.), the next step of D-MRI data analysis is often to summarize these measurements into some form of estimates of water diffusion at each voxel.

One of the earliest, and still popular, model for water diffusion is the so called single $tensor\ model$ where the diffusion process is modeled as a 3D Gaussian process described by a 3×3 positive definite matrix, referred to as a diffusion tensor (Mori, 2007). The voxel-level diffusion direction is extracted as the principal eigenvector of the (estimated) diffusion tensor. The white matter fiber tracts are then reconstructed by computer-aided tracking

algorithms via a process called tractography (Basser et al., 2000). As the tensor has only six parameters, the single tensor model can be fitted with as little as measurements along seven gradient directions.

Despite its simplicity and popularity, the single tensor model cannot resolve crossing fibers – multiple fiber populations with distinct orientations within a voxel – which are present in approximately 30% white matter voxels. Consequently, in crossing fiber regions, diffusion tensors tend to be estimated as oblate. This leads to early termination of or biased fiber tracking as well as misleadingly low anisotropic measures so that crossing fiber regions may be mistaken as CSF or grey matter regions.

In order to resolve intravoxel orientational heterogeneity, various models have been proposed including the multiple tensor model (Tuch et al., 2002; Scherrer and Warfield, 2010; Wong et al., 2016) and nonparametric models such as orientation distribution function (ODF) (Descoteaux et al., 2007) and fiber orientation distribution (FOD) (Tuch, 1996). To fit these models, high angular resolution diffusion imaging (HARDI) data (Tuch et al., 2002; Hosey et al., 2005) are often required where a large number of gradients is sampled on either one or multiple shells. Among these models, the FOD model directly describes the local spatial arrangement of axonal fiber bundles in such a way that sharply-defined geometric features are preserved (Jensen et al., 2016). This property makes the FOD an attractive representation of local neuronal fiber information particularly when the downstream goal is neuronal fiber reconstruction. More specifically, the FOD model assumes that the diffusion signal at each voxel is a spherical convolution between the response function – a kernel that characterizes water diffusion when there is a single dominant fiber bundle aligned with the z-axis, and the FOD function – a spherical probability density function for the neuronal fiber bundle orientation at that voxel. Estimating FOD based on observed D-MRI data

(i.e. noisy samples of the diffusion signal) is an ill-posed inverse problem and is subject to noise amplification. Therefore, appropriate regularization is the key for accurate FOD estimation.

In this paper, we propose a blockwise James-Stein type shrinkage method, referred to as BJS, for FOD estimation. BJS is based on spherical harmonics (SH) basis representation of FOD and includes four steps: (i) pre-conditioning which modulates the observations through a power of the SH coefficients of the convolution kernel and mitigates the degree of ill-conditioning of the deconvolution problem; (ii) blockwise shrinkage which applies a James-Stein type shrinkage of SH coefficients within each harmonics level (referred to as a block); (iii) post-processing which is applied to the shrunken pre-conditioned observations to remove the modulation effect of the convolution kernel on the underlying SH coefficients of the FOD; (iv) one-step sharpening which enhances localized peaks of the estimated FOD and thus further improves the accuracy.

We conduct extensive synthetic experiments and compare **BJS** with two other SH representation-based methods, namely, **SHridge** which uses a ridge-type penalty, and **SCSD** which applies an iterative super-resolution sharpening up on the **SHridge** estimator. The results demonstrate that **BJS** achieves similar accuracy as **SCSD** (and both are better than **SHridge**), and **BJS** is at least 10 times faster than the other two methods. Therefore, **BJS** is computationally scalable for analysis involving a large number of D-MRI images.

In this paper, we apply **BJS** to D-MRI data from 245 HCP young adult subjects. After estimation FOD in seven sub-cortical regions, we extract fiber direction information at each voxel using a peak detection algorithm (Yan et al., 2018) and then use the extracted directions as inputs in a fiber tracking algorithm (Wong et al., 2016) for white matter fiber

tracts reconstruction. We then extract the number of fibers (of a certain length) within each sub-cortical region and relate this feature to gender and handedness. We find significant gender main effects on the number of fibers within six subcortical regions. We also find significant gender-handedness interaction effects in two subcortical regions (Hippocampus and Amygdala).

The rest of the paper is organized as follows. Section 2 provides a description of the proposed **BJS** method. In Section 3, the performance of **BJS** is compared with two competing methods through synthetic experiments. Section 4 reports the results of applying **BJS** to HCP young adults data. We conclude the paper with discussion in Section 5. Further details can be referred to Supplementary Material.

2 Methodology

In this section, we describe in detail the proposed **BJS** method for FOD estimation. D-MRI utilizes the diffusion process of water molecule to probe architecture of biological tissues. Under the assumption that the observed diffusion weighted measurements at each voxel result from an FOD function blurred by the water diffusion process, one may employ the deconvolution operation to recover the FOD. On one hand, in order to achieve sufficient angular resolution, higher order harmonics are needed to represent FOD. On the other hand, deconvolution becomes increasingly instable and more susceptible to noise amplification as higher order harmonics are used in FOD representation, due to the rapid decay of the singular values of the design matrix.

To tackle this ill-conditioned inverse problem, we employ a blockwise James-Stein type shrinkage method. Blockwise nonlinear shrinkage strategies have been used in the literature for adaptive estimation in nonparametric regression (Cai, 1999; Cai et al., 2009) and linear inverse problems (Cavalier and Tsybakov, 2001, 2002), under the setting of i.i.d. noise. The major challenge in the current application, is that the design matrix for the observations does not diagonalize in the same basis as the convolution operator due to the limitations of the sampling design.

In BJS, we partition the observations into blocks corresponding to the frequency level of the SH basis. The rationale is that the SH transform of the convolution kernel (i.e., the response function) is constant within each harmonic frequency level and consequently, the covariance matrix of the observations within each block has more homogeneous diagonals and is less ill-conditioned. A James-Stein type shrinkage estimator is then applied within The original James-Stein shrinkage method is for estimating the mean of a Normal random vector where the coordinates are independent with a common (known) variance. Here, a careful modification of the shrinkage factor within each block is necessary to account for a lack of independence among the noise terms. Inspired by the proposals from Laurent and Massart (2000) and Cavalier and Tsybakov (2001), we adopt a more heavily penalized version of the James-Stein shrinkage which accounts for non-isotropic covariance of the observations, thus allowing heteroscedasticity as well as correlation among the observations. Moreover, the dimension of each block is used to determine the shrinkage factor, which is chosen in a way such that the probability of the ℓ_2 norm of the observations within the block exceeding the shrinkage threshold is small when there is no signal (i.e., when the SH coefficients of the FOD corresponding to this block are zero). In particular, for blocks corresponding to higher SH levels, larger shrinkage is used so that noise is more aggressively suppressed.

In addition to the James-Stein shrinkage, we also employ a pre-conditioning step to

mitigate the degree of ill-conditioning, as well as a post-estimation one-step super resolution sharpening to enhance the localized peaks of the estimated FOD. Since **BJS** does not involve any grid search or iteration, it is computationally very efficient and scales well for processing large number of diffusion weighted images.

In the following, we first introduce the spherical convolution model and SH representation for FOD and then detail the **BJS** steps.

2.1 SH Representation of FOD

The diffusion MRI signal function $S(\cdot)$ at each voxel is modeled as a spherical convolution of FOD $F(\cdot)$ with an axially symmetric convolution kernel $R(\cdot)$ (Tournier et al., 2004):

$$S(\mathbf{x}) = \int_{\mathbb{S}^2} R(\mathbf{x}^T \mathbf{y}) F(\mathbf{y}) d\omega(\mathbf{y}), \qquad \mathbf{x} \in \mathbb{S}^2,$$
 (1)

where $d\omega(\mathbf{y})$ is the volume element of \mathbb{S}^2 . In the above, $F(\cdot)$ is a symmetric spherical probability density function of the fiber bundle orientation population at this voxel and $R(\cdot)$ reflects the diffusion property of water molecule along a single dominant fiber bundle aligned with the z-axis. $R(\cdot)$ is referred to as the response function and is assumed to be the same across all voxels and fiber bundles. In practice, we may assume that $R(\cdot)$ belongs to a parametric family of nonnegative functions (e.g., specified by a tensor model) and then estimate the parameters based on voxels with a single dominant fiber bundle, typically characterized by high fractional anisotropy (FA) values under the single tensor model (Yan et al., 2018). In the following, $R(\cdot)$ is assumed to be given.

Since $S(\cdot)$, $F(\cdot)$ and $R(\cdot)$ are real and symmetric, they can be represented by real symmetrized spherical harmonic (SH) basis. Let $\{\widetilde{\Phi}_{lm}: -l \leq m \leq l; l = 0, 1, \ldots\}$ denote the complex SH basis. Then, a real symmetrized SH basis is defined as (Descoteaux et al.,

2007):

$$\Phi_{lm} = \begin{cases}
\sqrt{2} \cdot \Re(\widetilde{\Phi}_{lm}), & \text{if } -l \leq m < 0 \\
\Phi_{l0}, & \text{if } m = 0 \\
\sqrt{2} \cdot \Im(\widetilde{\Phi}_{lm}), & \text{if } 0 < m \leq l
\end{cases}$$
(2)

for l = 0, 2, 4, ..., where $\Re(z)$ and $\Im(z)$ denote the real and imaginary parts of $z \in \mathbb{C}$, respectively.

Since the response function $R(\cdot)$ is axially symmetric, $\langle R, \Phi_{lm} \rangle = 0$ unless m = 0. Let $r_l = \langle R, \Phi_{l0} \rangle$ and $f_{lm} = \langle F, \Phi_{lm} \rangle$ be the SH coefficients of $R(\cdot)$ and $F(\cdot)$, respectively. Then, by equation (1), the diffusion MR signal $S(\cdot)$ has SH coefficients:

$$s_{lm} = \langle S, \Phi_{lm} \rangle = \sqrt{\frac{4\pi}{2l+1}} r_l f_{lm}, -l \le m \le l; \quad l = 0, 2, \dots$$
 (3)

The observed data $\{y_i\}_{i=1}^n$ are noise corrupted versions of $S(\cdot)$ sampled at n diffusion gradient directions, $\mathbf{x}_i \equiv (\theta_i, \phi_i)$, i = 1, ..., n, where θ_i and ϕ_i are elevation angle and azimuthal angle of the ith gradient direction, respectively. Under the assumption that a finite level (up to l_{max}) of SH basis can represent $S(\cdot)$ and $F(\cdot)$, the observations can be modeled as:

$$\mathbf{y} = \mathbf{\Phi} \mathbf{R} \mathbf{f} + \boldsymbol{\varepsilon}, \quad \boldsymbol{\varepsilon} \sim N(0, \sigma_{\varepsilon}^2 \mathbf{I}_n),$$
 (4)

where \mathbf{R} is an $L \times L$ diagonal matrix with l-th diagonal block equal to $r_l \sqrt{4\pi/(2l+1)} \mathbf{I}_{2l+1}$, for $l = 0, 2, \ldots, l_{\text{max}}$ and $L = \frac{(l_{\text{max}}+1)(l_{\text{max}}+2)}{2}$ is the total number of SH basis; and $\boldsymbol{\Phi}$ is the $n \times L$ matrix with the elements in the i-th row and (l, m)-th column given by $\Phi_{lm}(\theta_i, \phi_i)$; and $\mathbf{f} = (f_{lm})$ is the $L \times 1$ vector of SH coefficients of the FOD $F(\cdot)$. Moreover, the vector $\boldsymbol{\varepsilon} = (\varepsilon_i)_{i=1}^n$ represents observational noise and is assumed to have independent coordinates that satisfy $\mathbb{E}(\varepsilon_i) = 0$ and $\mathrm{Var}(\varepsilon_i) = \sigma_{\varepsilon}^2$.

2.2 Blockwise James-Stein Shrinkage Estimator of FOD

Assume n > L, which implies that (a) $\mathbf{\Phi}^T \mathbf{\Phi}$ is well-conditioned (assuming a weak requirement on the configuration of the magnetic gradients at which D-MRI measurements are sampled); and (b) $\mathbf{R}^T \mathbf{\Phi}^T \mathbf{\Phi} \mathbf{R}$ is nonsingular. However, $\mathbf{\Phi}^T \mathbf{\Phi}$ is not the identity matrix. Also, for larger L, the matrix \mathbf{R} and consequently, the matrix $\mathbf{R}^T \mathbf{\Phi}^T \mathbf{\Phi} \mathbf{R}$ becomes significantly ill-conditioned, since r_l tends to zero as l increases. Therefore, a linear estimator of FOD (e.g. by ridge regression with Laplacian penalty – **SHridge**) is likely to produce poor results. In addition, since the FOD is expected to have only a few sharp peaks or no peak at all, but otherwise a smooth function, we can expect relatively large coefficients for low level harmonics and relatively small coefficients for high level harmonics. Therefore, a nonlinear shrinkage procedure with a blockwise adaptive choice of the shrinkage parameter is appropriate. Moreover, to further mitigate the ill-conditioning, the square root of the inverse of the matrix \mathbf{R} is applied to the observations in a preconditioning step before applying the blokwise shrinkage, and another square root of the inverse of \mathbf{R} is applied following the shrinkage to obtain the estimated SH coefficients of FOD. Finally, a one-step super resolution sharpening is used to enhance localized peaks of the estimated FOD.

The **BJS** method is described as follows:

Step 1: Preconditioning

In this step, we modulate the observations through preconditioning such that the covariance matrix of the observations is less ill-conditioned.

Define $\mathbf{R}^{\frac{1}{2}} = \operatorname{diag}(\operatorname{sign}(d_i)|d_i|^{\frac{1}{2}})_{i=1}^L$ and $\bar{\mathbf{R}}^{\frac{1}{2}} = \operatorname{diag}(|d_i|^{\frac{1}{2}})_{i=1}^L$, where d_i is the i-th diagonal element of \mathbf{R} . Then, $\mathbf{R}^{\frac{1}{2}}\bar{\mathbf{R}}^{\frac{1}{2}} = \bar{\mathbf{R}}^{\frac{1}{2}}\mathbf{R}^{\frac{1}{2}} = \mathbf{R}$. Let $\mathbf{K} = \bar{\mathbf{R}}^{-\frac{1}{2}}(\mathbf{\Phi}^T\mathbf{\Phi})^{-1}\mathbf{\Phi}^T$ be the preconditioning matrix. Multiplying \mathbf{K} to both sides of (4) to obtain the preconditioned

observations:

$$\mathbf{z} = \mathbf{K}\mathbf{y} = \mathbf{R}^{\frac{1}{2}}\mathbf{f} + \mathbf{K}\boldsymbol{\varepsilon} = \boldsymbol{\theta} + \mathbf{K}\boldsymbol{\varepsilon},\tag{5}$$

where $\boldsymbol{\theta} := \mathbf{R}^{\frac{1}{2}}\mathbf{f}$ and

$$Var(\mathbf{z}) = \sigma_{\varepsilon}^{2} \mathbf{K} \mathbf{K}^{T} = \sigma_{\varepsilon}^{2} \bar{\mathbf{R}}^{-\frac{1}{2}} (\mathbf{\Phi}^{T} \mathbf{\Phi})^{-1} \bar{\mathbf{R}}^{-\frac{1}{2}} = \sigma_{\varepsilon}^{2} \mathbf{V}$$

Step 2: Blockwise James-Stein Shrinkage

In this step, we estimate θ through a blockwise James-Stein type estimator by applying adaptive nonlinear shrinkage within each block.

Denote the block of $\boldsymbol{\theta}$ and \mathbf{z} corresponding to the l-th level SH basis by $\boldsymbol{\theta}^{(l)}$ and $\mathbf{z}^{(l)}$, respectively. The l-th block consists of (2l+1) coordinates of the respective vector for $l=0,2,4,...,l_{\text{max}}$ and there are $1+\frac{l_{\text{max}}}{2}$ total blocks. Let $\mathbf{V}^{(l)}$ be the corresponding $(2l+1)\times(2l+1)$ submatrix of \mathbf{V} and $\boldsymbol{\eta}^{(l)}$ be the l-th block of the transformed noise vector $\mathbf{K}\varepsilon$. Note that, $\boldsymbol{\eta}^{(l)}$ follows $N(0,\sigma_{\varepsilon}^2\mathbf{V}^{(l)})$.

For each level l, we have $\mathbf{z}^{(l)} = \boldsymbol{\theta}^{(l)} + \boldsymbol{\eta}^{(l)}$. We adopt a modified version of James-Stein shrinkage, which accounts for the non-isotropic covariance of $\boldsymbol{\eta}^{(l)}$. Specifically, the adaptive nonlinear shrinkage factor can be determined by making use of Lemma 2.1 below, as well as the representation,

$$\| \boldsymbol{\eta}^{(l)} \|_2^2 \sim \sigma_{\varepsilon}^2 \sum_{i=1}^{2l+1} \lambda_{l,i} w_{l,i}^2,$$

where $\lambda_{l,i}$ is the *i*-th largest eigenvalue of $\mathbf{V}^{(l)}$, and $w_{l,i} \sim N(0,1)$.

Lemma 2.1 (Laurent and Massart, 2000) Let $(w_1, ..., w_n)$ be i.i.d Gaussian variables, with mean 0 and variance 1 and $\lambda_1, ..., \lambda_n$ be nonnegative. We set

$$\|oldsymbol{\lambda}\|_{\infty} = \sup_{i=1,...,n} |\lambda_i|, \quad \|oldsymbol{\lambda}\|_2 = \sqrt{\sum_{i=1}^n \lambda_i^2}, \quad \|oldsymbol{\lambda}\|_1 = \sum_{i=1}^n |\lambda_i|$$

Then, the following inequality holds for any positive t:

$$P(\sum_{i=1}^{n} \lambda_i w_i^2 \ge \|\boldsymbol{\lambda}\|_1 + 2\|\boldsymbol{\lambda}\|_2 \sqrt{t} + 2\|\boldsymbol{\lambda}\|_{\infty} t) \le \exp(-t)$$

The above tail-probability bound for quadratic forms of Gaussian vectors motivates the following modified version of the positive-part James-Stein shrinkage estimator for $\boldsymbol{\theta}^{(l)}$

$$\hat{\boldsymbol{\theta}}^{(l)} = \left(1 - \frac{\hat{\sigma}_{\varepsilon}^{2}(\|\boldsymbol{\lambda}_{l}\|_{1} + 2\|\boldsymbol{\lambda}_{l}\|_{2}\sqrt{t^{(l)}} + 2\|\boldsymbol{\lambda}_{l}\|_{\infty}t^{(l)})}{\|\mathbf{z}^{(l)}\|_{2}^{2}}\right) \mathbf{z}^{(l)},$$
(6)

where λ_l is the vector of ordered eigenvalues of $\mathbf{V}^{(l)}$, $t^{(l)} \geq 0$ is a regularization parameter, and the error variance σ_{ε}^2 is estimated by the mean squared error (MSE) of the ordinary least square (OLS):

$$\hat{\sigma}_{\varepsilon}^{2} = \frac{\|\mathbf{y} - \mathbf{\Phi}(\mathbf{\Phi}^{T}\mathbf{\Phi})^{-1}\mathbf{\Phi}\mathbf{y}\|}{n - \operatorname{rank}(\mathbf{\Phi})}.$$

Note that, even though we have an ill-conditioned system, we can still get a good fit of the observations by OLS and consequently a good estimate of the error variance.

Finally, the above shrinkage is applied to all levels except for $l = 0, 2, ..., l_0$ for some $l_0 \ge 2$ (even). That is, for $l \le l_0$, $\hat{\boldsymbol{\theta}}^{(l)} = \mathbf{z}^{(l)}$. In this paper, we set $l_0 = 4$.

Steps 3 & 4: Postprocessing and Sharpening

The estimated SH coefficients for FOD is obtained by:

$$\hat{f} = \mathbf{R}^{-\frac{1}{2}}\hat{\boldsymbol{\theta}} \tag{7}$$

and the evaluation of the estimated FOD on an arbitrary grid is given by $\hat{F} = \tilde{\Phi}\hat{f}$, where $\tilde{\Phi}$ is an $\tilde{n} \times L$ matrix representing the evaluation of the L SH basis on this grid.

Since the estimated FOD may have negative values caused by artificial oscillations, to impose nonnegativity, \hat{f} is further updated through a one-step super-resolution sharpening

which sharpens the peak and suppresses negative values. Details of the sharpening step are available in Supplementary Material.

Rationale behind the James-Stein shrinkage factor

Our formulation of the blockwise shrinkage factor explicitly accounts for the correlation among coefficients within each block and heteroscedastic noise. In particular, the shrinkage parameters are set as $t^{(l)} = 2\log(2l+1)$, which ensure that if a block contains no signal, then its estimate will be set to zero with probability tending to one, by Lemma 2.1 and the Borel-Cantelli lemma.

Cavalier and Tsybakov (2001) solved a linear inverse problem under a Gaussian sequence model with i.i.d. noise, using a blockwise James-Stein shrinkage rule. They first converted the inverse problem to a direct estimation problem with independent but heteroscedastic noise. They showed that a larger value of the threshold than in the ordinary James-Stein shrinkage procedure gave better control on the variance at the expense of slightly increased bias. In our context, we also deal with an inverse problem, by first employing a half-inversion of the convolution operator, followed by the application of blockwise James-Stein procedure, and finally another half-inversion of the convolution operator (see equation (7)) to obtain the estimates of the SH coefficients of the FOD. Therefore, a better control of the variance within each block is of greater significance. This is because, without a stronger control of the variance, the final post-processing operation can significantly amplify noise in the estimate.

In a closely related setting, though concerning a direct rather than an inverse regression problem involving orthogonal regressors and correlated Gaussian noise, Goldenshluger and Tsybakov (2001) showed that the standard James-Stein estimator still has theoretically

near-optimal risk performance (in comparison with the linear oracle estimator) as long as the correlation is mild. In our context, empirical analyses show that, for the sampling design we consider, each block of the noise covariance matrix \mathbf{V} is quite well-conditioned even for higher SH level l (condition number is close to 1 for l=4 and less than 1.2 for l=10), while the maximum absolute correlation among the coefficients within each block is modest (around 0.3). Thus, our choice of the shrinkage factor can be seen as a hybrid addressing the combined scenarios dealt with by Cavalier and Tsybakov (2001) and Goldenshluger and Tsybakov (2001). This explains the satisfactory empirical risk behavior of our proposed estimator.

2.3 Other FOD Estimators

For comparison purpose, we consider two methods which also use SH basis for FOD estimation.

SHridge Estimator

The **SHridge** estimator is motivated by Descoteaux et al. (2006) who proposed the Laplace-Beltrami regularization to estimate diffusion orientation distribution function (dODF). The same penalty can be used for FOD estimation (Yan et al., 2018):

$$\min_{f} ||\mathbf{y} - \mathbf{\Phi} \mathbf{R} \mathbf{f}||_{2}^{2} + \lambda \mathbb{E}(F), \quad \mathbb{E}(F) := \int_{\Omega} (\triangle_{b} F)^{2} d\Omega = \mathbf{f}^{T} \mathbf{P} \mathbf{f},$$
 (8)

where **P** is a block diagonal matrix with entries $l^2(l+1)^2$ corresponding block size 2l+1 for $l=0,2,\ldots,l_{\text{max}}$; Δ_b is the spherical Laplacian operator, and $\mathbb{E}(F)$ is a measure of roughness of spherical functions. With the objective function (8), The estimated coefficients of FOD

are:

$$\hat{\mathbf{f}}^{SHridge} = (\mathbf{R}^T \mathbf{\Phi}^T \mathbf{\Phi} \mathbf{R} + \lambda \mathbf{P})^{-1} \mathbf{R}^T \mathbf{\Phi}^T \mathbf{y}. \tag{9}$$

The tuning parameter λ can be chosen by grid search and the Bayesian information criterion (BIC).

SCSD Estimator

The superCSD procedure is proposed by Tournier et al. (2007). It aims to sharpen the peak(s) of an estimated FOD and alleviates the Gibbs phenomenon by forcing small positive values as well as negative values to be zero through an SH representation of high order l_{max}^s and an iterative updating. We refer to the superCSD procedure applied to the **SHridge** estimator as **SCSD**. In this paper, $l_{\text{max}}^s = 16$ is used for the synthetic experiments with separation angle 30°. For all other cases and the real data application, $l_{\text{max}}^s = 12$ is used. Other parameters of the superCSD procedure are set at the recommended values as in Tournier et al. (2007).

Remarks

Both **BJS** and **SCSD** use the super-resolution sharpening process. However, **BJS** uses super-resolution sharpening only once to suppress the negative values of the estimated FOD, whereas **SCSD** suppresses both negative and small positive values iteratively until there is no significant change in the estimated coefficients of FOD. Consequently, **SCSD** is more computationally costly than **BJS**.

3 Synthetic Experiments

The performance of **BJS** is assessed through extensive synthetic experiments. Synthetic data is generated under the multi-tensor model with different settings in terms of the number of fibers, separation angles between fibers, the number of gradient directions, b-value, and signal-to-noise ratio (SNR). The performance of **BJS** is also compared with **SHridge** and **SCSD**.

3.1 Experimental Setting

In terms of the number of fibers and the separation angles, we consider single fiber, two fibers with 5 different separation angles (30°, 45°, 60°, 75°, 90°), and three fibers with 2 different separation angles (60°, 90°). Also, two different b-values $1,000s/mm^2$, $3,000s/mm^2$, a key parameter in diffusion MRI experiments, are considered. The higher the b-value, the more sensitive of the diffusion measurements to the water molecule movement in the brain. Moreover, diffusion signals are sampled from, n = 41, 91, 321, respectively, gradient directions on equiangular grids. Lastly, two different levels of SNR (20,50), are used for data generation. Here, SNR is defined as the ratio of the non-diffusion weighted signal intensity S_0 to the standard deviation of the Rician noise. For each setting, 100 sets of diffusion weighted measurements are generated by adding the Rician noise to the noiseless diffusion signal under the multi-tensor model.

The synthetic experiments cover the settings commonly used in both clinical and research purpose HARDI experiments. Especially, the HCP data have 90 gradient directions at b-value $3{,}000s/mm^2$ and a median of SNR about 50 (Figure S4).

3.2 Running Time Comparison

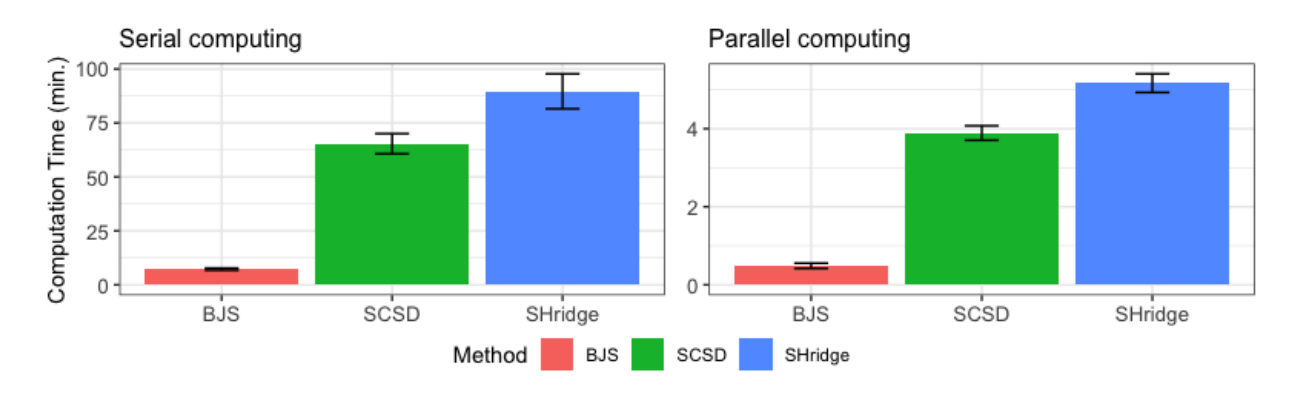


Figure 1: Execution time (across 30 replicates): 100,000 voxels, 91 gradient directions, $l_{\text{max}} = l_{\text{max}}^s = 10$. Left panel – serial computing. Right panel – parallel computing with 30 cores.

The execution time of the three methods is evaluated on a server with Xeon 72 core processor, 2.3GHz, 256GB RAM. For **SHridge**, a grid with 100 values is used for tuning parameter selection (with BIC). For **SCSD**, the estimates from **SHridge** are used as initial estimates.

The running time is averaged across 30 simulation replicates, where in each set every method processes 100k voxels which is on a par with the number of white matter voxels in real D-MRI data. Figure 1 shows that **BJS** is at least 10 times faster than the other two methods in both serial and parallel (30 cores) computing.

Note that, the running time of **SHridge** is highly dependent on the size of the tuning grid.

3.3 Evaluation Metrics

The performance of each method is evaluated with the detection rate (D.R.) and the mean estimated separation angle (Tables S1, S2, S3, S4). The detection rate is the percentage across the 100 replicates where the peak detection algorithm (Yan et al., 2018) finds the correct number of fibers. Also, when the number of fibers is correctly detected, the estimated separation angle between pairs of fibers is obtained. Moreover, the estimated FODs are visualized and directly compared with the true FOD directions (Figures 2, S1, S2, S3), where the opaque color represents the mean of the estimated FOD (across 100 replicates) and semitranslucent color represents the mean plus two standard deviations of the estimated FODs.

3.4 Results

Only the graphical results at separation angle 45° are reported in the main text (Figure 2), while other results are available in Supplementary Material (Figures S1, S2 and S3, and Tables S1, S2, S3, S4).

In the case of two fibers with separation angle 30° , none of the methods performs well with $l_{\text{max}}^{s} = 12$. However, when b-value is $3{,}000s/mm^{2}$ and $l_{\text{max}}^{s} = 16$, BJS outperforms both SCSD and SHridge (Figure S1 and Table S1). In terms of detection rates, the performance of BJS is almost twice as good as SCSD and is much better than SHridge. With SNR = 50, the detection rate of BJS improves a little bit compared to the case of SNR = 20. For both SNR = 20 and SNR = 50, the estimated separation angle is very close to the true separation angle 30° . On the other hand, SCSD tends to underestimate the separation angle.

For the case of two fibers with separation angle 45° (Figure 2 and Table S2), **SHridge** shows poor performance except for $b = 3{,}000s/mm^2$, SNR = 50 and n = 321. Both **BJS** and **SCSD** successfully identify two fibers with $b = 3{,}000s/mm^2$. However, the estimated separation angle of **BJS** is much closer to the true separation angle 45° than that of **SCSD**.

In case of two fibers with moderate to large separate angles $(60^{\circ}, 75^{\circ}, 90^{\circ})$ (Figure S2 and Table S3), and three fibers with separation angle 60° or 90° (Figure S3 and Table S4), **BJS** and **SCSD** show comparable performance and both are better than **SHridge**. However, for separation angle 60° and SNR = 20, the detection rate of **BJS** is almost twice as good as **SCSD**)

In summary, when the separation angle is small, **BJS** outperforms **SCSD**. Overall, **BJS** shows more accurate estimation than **SCSD** and **SHridge**.

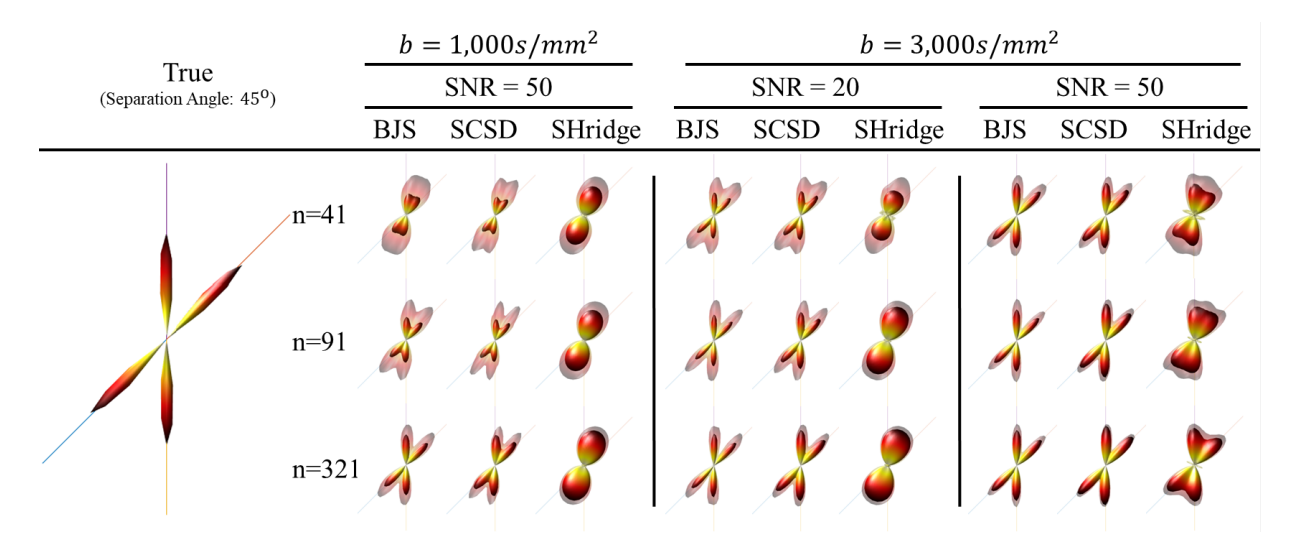


Figure 2: Two fibers with separation angle 45°. The solid lines are the true fiber directions. The opaque part and the semitranslucent part represent the mean estimated FODs across 100 replicates and the mean plus two standard deviations of the estimated FODs.

4 HCP Young-Adult Application

4.1 Data Analysis Pipeline

In this section, we describe an application using HCP young adults data to investigate the association between brain structural connectivity and demographic and behavioral features, gender and handedness. The data analysis pipeline (with processing time per subject) is shown in Figure 3. Details are described as follows.

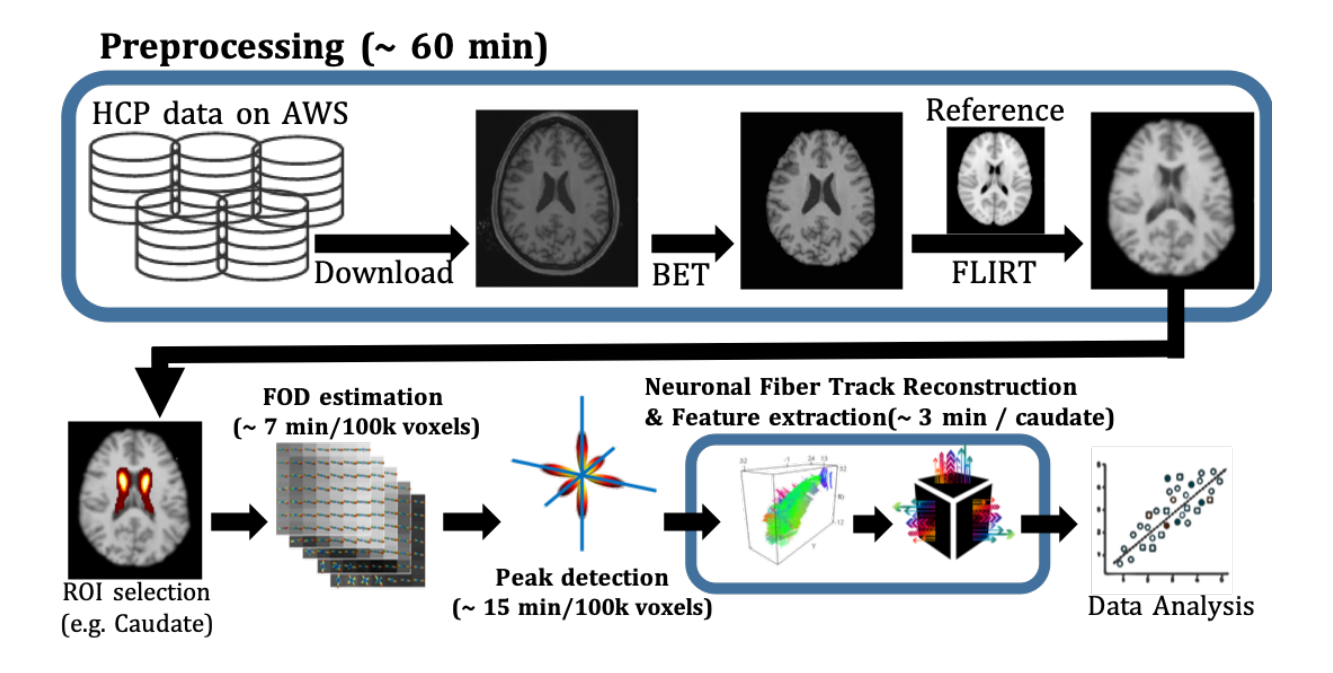


Figure 3: HCP young adults application: data analysis pipeline

The WU-Minn Human Connectome Project (HCP) (Essen et al., 2013) has eddy-current-corrected D-MRI data of 1206 healthy young adults (Age: $22 \sim 35$) from 457 unique families. D-MRI are taken at 3 different b-values $(1,000s/mm^2,2,000s/mm^2,3,000s/mm^2)$

on a $145 \times 174 \times 145$ grid with voxel size $1.25 \times 1.25 \times 1.25mm^3$. For each b-value, 90 gradient directions and 6 b_0 images are available. In the subsequent analysis, D-MRI with $b=3,000s/mm^2$ is used.

We classify the subjects into left hander (EHI: $-100 \sim -55$) and right hander (EHI: $85 \sim 100$) by handedness score measured using the Edinburgh Handedness Index (EHI). In order to remove family effect, we choose one subject from each family. If all subjects from a family are right handed, then a subject is randomly selected. Otherwise, priority is given to left handed members. Through the above sampling scheme, 245 subjects (Male -92, Female -153; Left handed -48, Right handed -197) are sampled (Figure 4).

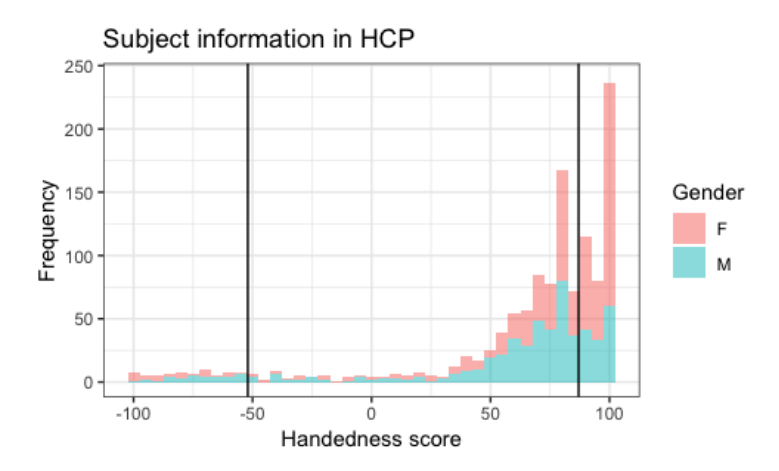


Figure 4: Handedness and Gender distribution in HCP young adults data. The two vertical lines correspond to the handedness thresholds used in this paper.

The original D-MRI are preprocessed with FSL version 6.0.0 (Jenkinson et al., 2012). The preprocessing involves the Brain Extraction tool (BET) and FMRIB's Linear Image Registration Tool (FLIRT). We use MNI152 brain template to register each individual's brain to the same space via intensity based 12 affine transformation. After preprocessing,

each image is on a $90 \times 108 \times 90$ grid with voxel size $2 \times 2 \times 2mm^3$.

To estimate the response function (convolution kernel), for each image, 60,000 voxels are processed in the registered space. At each voxel, the fractional anisotropy (FA) is estimated under the single tensor model. Following (Yan et al., 2018), we assume that a voxel with FA value greater than 0.8 and the ratio between the two minor eigenvalues less than 1.5 is a voxel with a single dominant fiber bundle. These voxels are then used to estimate the ratio between the major eigenvalue and the minor eigenvalue of the response function. In addition, the signal to noise ratio (SNR) is estimated by using the 6 b_0 images and taken as the median of the signal to noise ratio (S_0/σ) over the same set of voxels. These estimates are reported in Figure S4.

Seven subcortical regions of interest (ROIs), namely Accumbens, Amygdala, Caudate, Hippocampus, Pallidum, Putamen and Thalamus, in both left and right hemispheres are selected based on *Havard-Oxford Subcortical Atlas* on the MNI152 brain template. These ROIs are shown on Figure 5, panels (a-f). Corresponding ROIs are then extracted on each subject's registered image. For each ROI of a subject, FOD at each voxel is estimated via **BJS**. Then the peaks of the estimated FODs are identified by a peak detection algorithm (Yan et al., 2018). The extracted peak directions are fed to a deterministic tracking algorithm **DiST** (Wong et al., 2016) to reconstruct neuronal fiber tracks within each ROI on the registered space of each subject. The reconstructed fiber tracts for one subject is illustrated in Figure 5, panels (g,h).

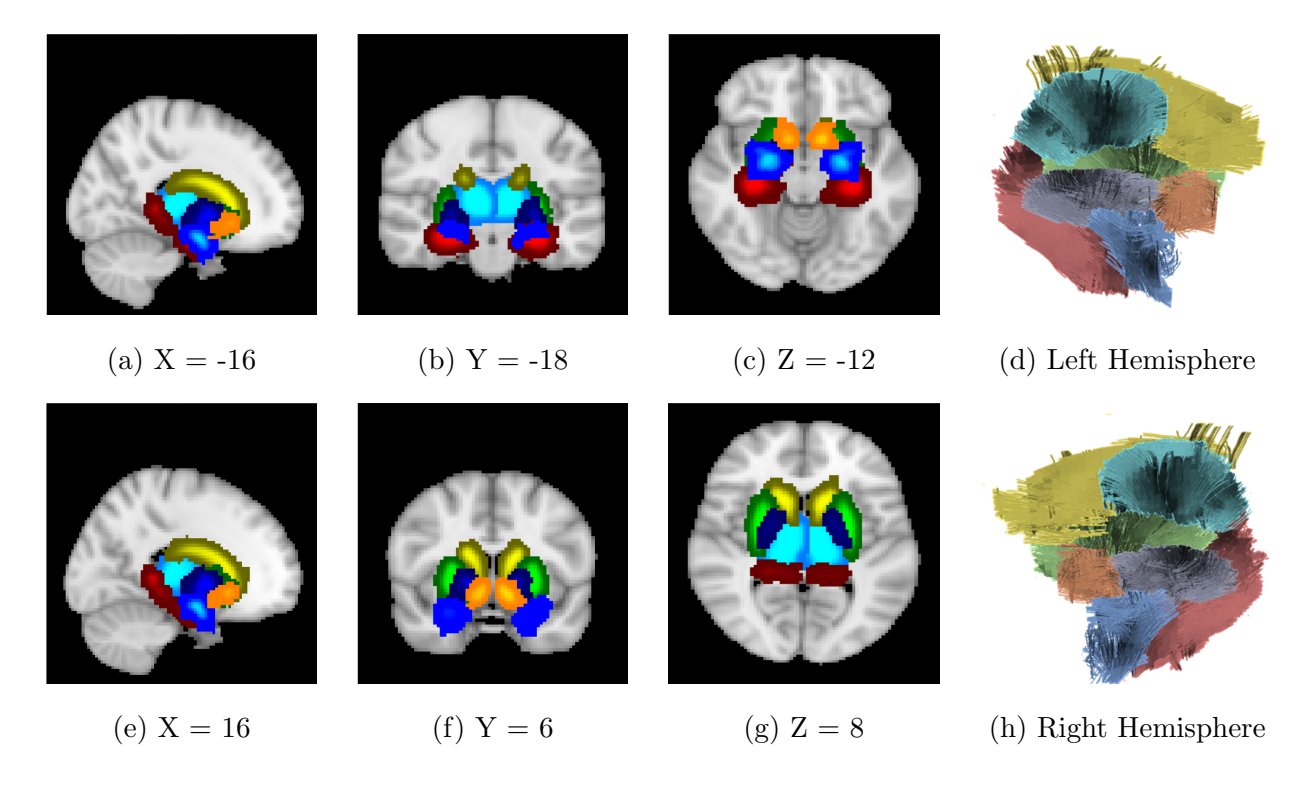


Figure 5: Panels (a-c, e-g): Selected subcortical ROIs from Havard-Oxford Subcortial Atlas: Accumbens(Orange), Amygdala(Blue), Caudate(Yellow), Hippocampus(Red), Pallidum(Navy), Putamen(Green), Thalamus(Lightblue). Panels (d,h): Reconstructed fiber tracks of one subject based on **BJS** FOD estimates, followed by peak detection and tractography.

We then use the number of estimated fiber tracks within each ROI (left hemisphere plus right hemisphere) as a brain structural connectivity feature. Specifically, within each subcortical ROI, we count the fibers whose length is greater than the 3rd quantiles of the fiber lengths across all subjects in that region. By excluding shorter fibers which are more likely to be spurious, we can expect less noisy and more reliable results. This extracted

feature is then used to investigate the association of brain structural connectivity with gender and handedness.

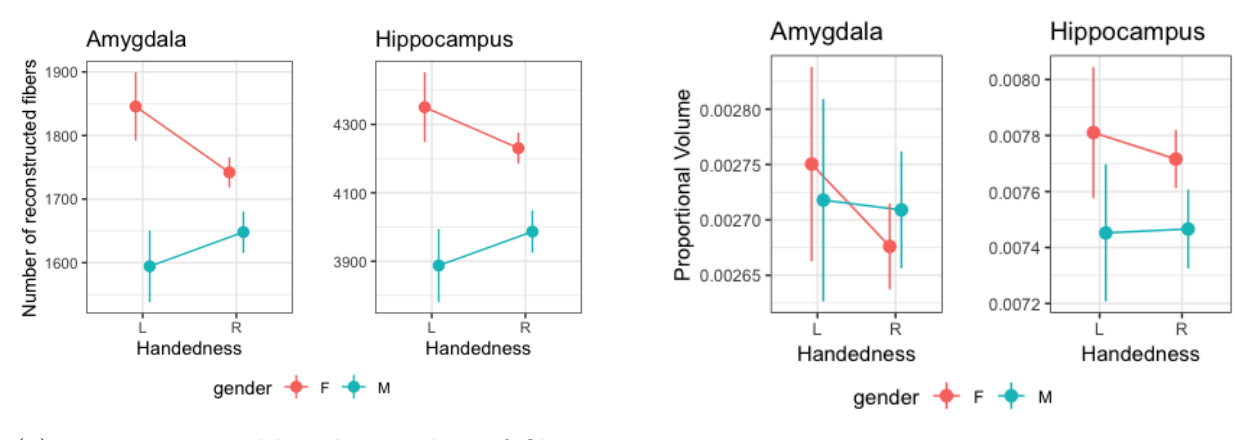
4.2 Results

It is widely known that the brain structures of males and females are different. For example, on average, males have larger brain volume than females. Most of the research that investigated gender effects on the structural organization of white matter used voxel-based morphometric (VBM) analysis (Herron et al., 2015; Jancke et al., 2015; Ritchie et al., 2018). In such studies, the compartment volume was also adjusted with respect to the total brain volume (Jancke et al., 2015; Ritchie et al., 2018). HCP data provides volumetric segmentation results based on *FreeSurfer* image analysis (Fischl et al., 2004). In the following, we also analyze the relationships between the proportional subcortical compartments volume (normalized by the total brain volume) with gender and handedness. Moreover, since the number of fibers is extracted from the tractography results reconstructed on a common template space, we can assume that the number of fibers has already been normalized according to brain size.

The two-way ANOVA results are reported in Tables 1 and S6 and Figure 6. For the number of fibers, gender has significant main effects in 6 out of 7 regions (except for Caudate). Moreover, there are significant interaction effects in Amygdala and Hippocampus. For proportional volume, the results show that 5 out of 7 regions (except for Amygdala and Accumbens) have significant gender main effects. This is consistent with Jancke et al. (2015) where it was reported that Amygdala does not have a significant gender effect in terms of proportional volume. However, no significant interaction between gender and handedness is observed with proportional volume.

Response Variable	Number of Fibers								
Factor	Gender (G)	Handedness (H)	(G) × (H)						
Accumbens	0.035	0.891	0.730						
Amygdala	0.000	0.891	0.003						
Caudate	0.071	0.891	0.229						
Hippocampus	0.000	0.891	0.036						
Pallidum	0.000	0.891	0.229						
Putamen	0.000	0.891	0.303						
Thalamus	0.000	0.891	0.294						

Table 1: Two-way ANOVA FDR adjusted pvalues: Response – the number of fibers within an ROI; Factors – gender, handedness



- (a) Response variable: the number of fibers within an ROI
- (b) Response variable: proportional volume of an ROI

Figure 6: Two-way ANOVA interaction plots: Factors – gender, handedness

5 Discussion

In this paper, we propose a new and computationally efficient method for estimating the fiber orientation distribution at each voxel using D-MRI data. Moreover, by using features derived from the estimated FODs, such as the number of fiber tracts within a subcortical region, we carry out ANOVA to study the association between the brain structure and gender and handedness of an individual.

The proposed **BJS** method is a computationally efficient, stable, non-iterative procedure for estimating the FOD. Particularly, this method is scalable for statistical analysis of brain connectivity at a population level. Moreover, the proposed **BJS** procedure constitutes an effective improvisation on the classical James-Stein shrinkage that solves an ill-conditioned inverse problem with noisy measurements in a non-standard setting where an exact diagonalization of the convolution operator in a basis representing the observation vector (D-MRI measurements) is not feasible due to the sampling design.

Finally, the statistical analysis based on HCP data is a demonstration of the potential benefits of utilizing brain connectivity features as predictors for behavioral traits of individuals. Particularly, we build a data analysis pipeline which can be utilized for extensive exploratory analysis of HCP data from the point of view of associative studies relating brain anatomic features to demographic and behavioral traits as well as cognitive measurements.

To reconstruct neuronal fiber tracts, the estimated FOD at each voxel need to provide reasonably accurate fiber orientation information. Based on synthetic experiment results, we believe that the estimated FODs via **BJS** are accurate enough to be used as inputs to a tracking algorithm. Although a large proportion of the neuronal fiber bundles can be explained by the reconstructed neuronal fiber tracks based on D-MRI, it is not sufficient to represent the actual fiber system in the brain. Also, the estimated fiber composition

can be different depending on the algorithm (Jones et al., 2013). Nevertheless, in a recent study about social anxiety disorder (SAD) (Baur et al., 2013), the authors investigated the association between SAD with the number of constructed white matter fiber tracts in the uncinate fasciculus (UF) and inferior fronto-occipital fasciculus based on DTI and probabilistic tracking algorithms. This paper further shows that it is possible to extract meaningful information from reconstructed neuronal fiber tracks based on D-MRI and to relate such information with external features.

Acknowledgments

We thank Hao Yan, Jilei Yang, and Raymond Wong for sharing codes for peak detection, fiber tracking and generating synthetic D-MRI data. Data were provided by the Human Connectome Project, WU-Minn Consortium (Principal Investigators: David Van Essen and Kamil Ugurbil; 1U54MH091657) funded by the 16 NIH Institutes and Centers that support the NIH Blueprint for Neuroscience Research; and by the McDonnell Center for Systems Neuroscience at Washington University.

References

Bammer, R., S. J. Holdsworth, W. B. Veldhuis, and S. Skare (2009). New methods in diffusion-weighted and diffusion tensor imaging. *Magnetic Resonance Imaging Clinics of North America* 17, 175–204.

Basser, P. J., S. Pajevic, C. Pierpaoli, J. Duda, and A. Aldroubi (2000). In vivo fiber tractography using DT-MRI data. *Magnetic Resonance in Medicine* 44(4), 625–632.

- Baur, V., A. B. Bruhl, U. Herwig, T. Eberle, M. Rufer, A. Delsignore, L. Jancke, and J. Hanggi (2013). Evidence of frontotemporal structural hypoconnectivity in social anxiety disorder: A quantitative fiber tractography study. *Human Brain Mapping* 34, 437–446.
- Beaulieu, C. (2002). The basis of anisotropic water diffusion in the nervous system a technical review. NMR in Biomedicine 15, 435–455.
- Cai, T. T. (1999). Adaptive wavelet estimation: a block thresholding and oracle inequality approach. *The Annals of Statistics* 27, 898–924.
- Cai, T. T., M. G. Low, and L. H. Zhao (2009). Sharp adaptive estimation by a blockwise method. *Journal of Nonparametric Statistics* 21, 839–850.
- Cavalier, L. and A. Tsybakov (2002). Sharp adaptation for inverse problems with random noise. *Probability Theory and Related Fields* 123, 323–354.
- Cavalier, L. and A. B. Tsybakov (2001). Penalized blockwise Stein's method, monotone oracles and sharp adaptive estimation. *Mathematical Methods of Statistics* 10.
- Chanraud, S., N. Zahr, E. V. Sullivan, and A. Pfefferbaum (2010). MR diffusion tensor imaging: a window into white matter integrity of the working brain. *Neuropsychology Review* 20(2), 209–225.
- Descoteaux, M., E. Angelino, S. Fitzgibbons, and R. Deriche (2006). Apparent diffusion coefficients from high angular resolution diffusion imaging: Estimation and applications. Magnetic Resonance in Medicine 56, 395–410.

- Descoteaux, M., E. Angelino, S. Fitzgibbons, and R. Deriche (2007). Regularized, fast and robust analytical Q-ball imaging. *Magnetic Resonance in Medicine* 58, 497–510.
- Essen, D. C. V., S. M. Smith, D. M. Barch, T. E. Behrens, E. Yacoub, and K. Ugurbil (2013). The wu-minn human connectome project: An overview. *NeuroImage* 80, 62 79.
- Fischl, B., D. H. Salat, A. J. van der Kouwe, N. Makris, F. Sgonne, B. T. Quinn, and A. M. Dale (2004). Sequence-independent segmentation of magnetic resonance images. *NeuroImage* 23, S69 – S84.
- Goldenshluger, A. and A. Tsybakov (2001). Adaptive prediction and estimation in linear regression with infinitely many parameters. *The Annals of Statistics* 29, 1601–1619.
- Herron, T., X. Kang, and D. Woods (2015). Sex differences in cortical and subcortical human brain anatomy. F1000Research 4.
- Hosey, T., G. Williams, and R. Ansorge (2005). Inference of multiple fiber orientations in high angular resolution diffusion imaging. *Magnetic Resonance in Medicine* 54, 1480–1489.
- Jancke, L., S. Merillat, F. Liem, and J. Hanggi (2015). Brain size, sex, and the aging brain. Human Brain Mapping 36, 150–169.
- Jenkinson, M., C. F. Beckmann, T. E. Behrens, M. W. Woolrich, and S. M. Smith (2012). Fsl. NeuroImage 62, 782 790.
- Jensen, J. H., G. Russell Glenn, and J. A. Helpern (2016). Fiber ball imaging. *NeuroImage* 124, 824–833.

- Jones, D. K., T. R. Knsche, and R. Turner (2013). White matter integrity, fiber count, and other fallacies: The do's and don'ts of diffusion mri. *NeuroImage* 73, 239 254.
- Laurent, B. and P. Massart (2000). Adaptive estimation of a quadratic functional by model selection. *The Annals of Statistics* 28, 1302 1338.
- Le Bihan, D., J.-F. Mangin, C. Poupon, A. C. Clark, S. Pappata, N. Molko, and H. Chabriat (2001). Diffusion tensor imaging: concepts and applications. *Journal of Magnetic Resonance Imaging* 13, 534–546.
- Mori, S. (2007). Introduction to Diffusion Tensor Imaging. Elsevier.
- Mukherjee, P., J. I. Berman, S. W. Chung, C. Hess, and R. Henry (2008). Diffusion tensor MR imaging and fiber tractography: theoretic underpinnings. *American Journal of Neuroradiology* 29(4), 632–641.
- Ritchie, S. J., S. R. Cox, X. Shen, M. V. Lombardo, L. M. Reus, C. Alloza, M. A. Harris,
 H. L. Alderson, S. Hunter, E. Neilson, D. C. M. Liewald, B. Auyeung, H. C. Whalley,
 S. M. Lawrie, C. R. Gale, M. E. Bastin, A. M. McIntosh, and I. J. Deary (2018). Sex
 Differences in the Adult Human Brain: Evidence from 5216 UK Biobank Participants.
 Cerebral Cortex 28, 2959–2975.
- Scherrer, B. and S. K. Warfield (2010). Why multiple b-values are required for multi-tensor models. evaluation with a constrained log-euclidean model. In 2010 IEEE International Symposium on Biomedical Imaging: From Nano to Macro, pp. 1389–1392. IEEE.
- Tournier, J.-D., F. Calamante, and A. Connelly (2007). Robust determination of the fibre orientation distribution in diffusion mri: Non-negativity constrained super-resolved spherical deconvolution. *NeuroImage* 35, 1459 1472.

- Tournier, J.-D., F. Calamante, D. G. Gadian, and A. Connelly (2004). Direct estimation of the fiber orientation density function from diffusion-weighted mri data using spherical deconvolution. *NeuroImage* 23, 1176 1185.
- Tuch, D. S. (1996). Q-ball imaging. Magnetic Resonance in Medicine 52, 1358–1372.
- Tuch, D. S., T. G. Reese, M. R. Wiegell, N. Makris, J. W. Belliveau, and V. J. Wedeen (2002). High angular resolution diffusion imaging reveals intravoxel white matter fiber heterogeneity. *Magnetic Resonance in Medicine* 48, 577–582.
- Wong, R. K. W., T. C. M. Lee, D. Paul, and J. Peng (2016). Fiber direction estimation, smoothing and tracking in diffusion MRI. *The Annals of Applied Statistics* 10, 1137–1156.
- Yan, H., O. Carmichael, D. Paul, J. Peng, and ADNI (2018). Estimating fiber orientation distribution from diffusion MRI with spherical needlets. *Medical Image Analysis* 46, 57–72.

SUPPLEMENTARY MATERIAL

S.1 More details about BJS

BJS Steps 3 & 4: Postprocessing and Sharpening

The estimated SH coefficients for FOD is obtained by:

$$\hat{f} = \mathbf{R}^{-\frac{1}{2}}\hat{\boldsymbol{\theta}}.\tag{10}$$

The estimated FOD may have negative values caused by artificial oscillations. To impose nonnegativity, \hat{f} is further updated through a one-step super-resolution sharpening which sharpens the peak and suppresses negative values as described in the following.

Let $\hat{F} = \Phi_{n_d \times L} \hat{f}$ be the evaluation of the estimated FOD on a dense spherical grid (e.g., $n_d = 2562$). Let $J = \{i : \hat{F}_i < 0, i = 1, ..., n_d\}$, $|J| = n_{neg}$. Let L_s be the number of SH basis functions corresponding to l_{\max}^s order. Note that l_{\max}^s can be greater than the l_{\max} that is used to get \hat{f} . In this paper, we set $l_{\max} = 10$ (i.e., L = 66) and $l_{\max}^s = 12$ (i.e. $L_s = 91$). Let $\Phi_{n \times L_s}^s$ be the evaluation matrix of L_s SH basis functions on n gradient directions. Let $\Phi_{nneg \times L_s}^{neg}$ be the evaluation matrix of L_s SH basis functions on n_{neg} grid points corresponding to negative estimated FOD values. Let $\mathbf{R}_{L_s \times L_s}^s$ be the \mathbf{R} matrix corresponding to the l_{\max}^s order SH representation of the response function.

Then the updated estimates of SH coefficients of FOD is defined as:

$$\hat{\mathbf{f}}^{BJS} = (\tilde{\mathbf{Z}}^T \tilde{\mathbf{Z}})^{-1} \tilde{\mathbf{Z}}^T \tilde{\mathbf{y}},\tag{11}$$

where

$$ilde{\mathbf{y}} = egin{bmatrix} \mathbf{y} \ \mathbf{0} \end{bmatrix}, ilde{\mathbf{Z}}_{(n+n_{neg}) imes L_s} = egin{bmatrix} \mathbf{\Phi}^s \mathbf{R}^s \ \mathbf{\Phi}^{neg} \end{bmatrix}$$

S.2 More details about synthetic experiments

Two Fibers, Separation Angle 30°

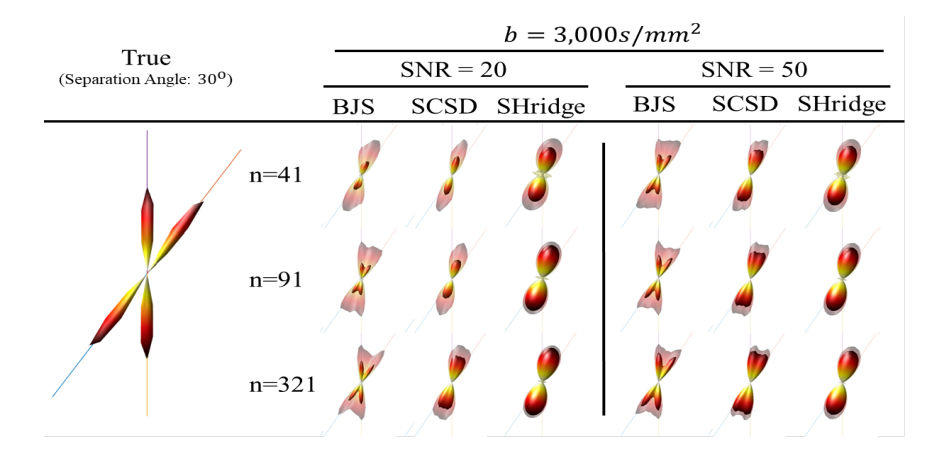


Figure S1: Two fibers with separation angle 30°. The solid lines are the true fiber directions. The opaque part and the semitranslucent part represent the mean estimated FODs across 100 replicates and the mean plus two standard deviations of the estimated FODs.

Settings	Design		BJS		SCSD	SHridge		
Settings	Design	D.R.	Mean(s.e)	D.R.	Mean(s.e.)	D.R.	Mean(s.e.)	
	$n = 41, l_{\text{max}} = 6, l_{\text{max}}^s = 16$	47%	31.598 (0.439)	23%	31.192 (0.638)	3%	63.396 (6.949)	
$b = 3000 \ s/mm^2, \ SNR = 20$	$n = 91, l_{\text{max}} = 10, l_{\text{max}}^s = 16$	68%	30.400 (0.391)	42%	28.667 (0.650)	1%	61.451 (-)	
	$n = 321, l_{\text{max}} = 12, l_{\text{max}}^s = 16$	82%	30.148 (0.335)	43%	25.360 (0.464)	0%	-	
$b = 3000 \ s/mm^2$, SNR = 50	$n = 41, l_{\text{max}} = 6, l_{\text{max}}^s = 16$	67%	28.982 (0.412)	15%	22.722 (1.112)	10%	71.923 (2.666)	
	$n = 91, l_{\text{max}} = 10, l_{\text{max}}^s = 16$	77%	28.823 (0.369)	39%	22.113 (0.646)	0%	=	
	$n = 321, l_{\text{max}} = 12, l_{\text{max}}^s = 16$	88%	28.111 (0.377)	56%	20.413 (0.535)	0%	-	

Table S1: The performance of three methods (**BJS**, **SCSC**, **SHridge**) for two fibers with separation angle 30°. The mean of estimated separation angle and the standard error with detection rates are reported under 6 different scenarios.

Two fibers, Separation Angle 45°

G.H.	Davion		BJS		SCSD	SHridge		
Settings	Design	D.R.	Mean(s.e)	D.R.	Mean(s.e.)	D.R.	Mean(s.e.)	
	$n = 41, l_{\text{max}} = 6, l_{\text{max}}^s = 12$	62%	43.673 (0.779)	82%	40.015 (0.374)	3%	74.370 (8.947)	
$b = 1000 \ s/mm^2, SNR = 50$	$n = 91, l_{\text{max}} = 10, l_{\text{max}}^s = 12$	83%	44.413 (0.589)	97%	40.400 (0.240)	0%	-	
	$n = 321, l_{\text{max}} = 12, l_{\text{max}}^s = 12$	100%	44.845 (0.310)	100%	40.167 (0.210)	0%	-	
	$n = 41, l_{\text{max}} = 6, l_{\text{max}}^s = 12$	92%	43.294 (0.612)	90%	41.277 (0.458)	2%	66.646 (16.053)	
$b = 3000 \ s/mm^2, SNR = 20$	$n = 91, l_{\text{max}} = 10, l_{\text{max}}^s = 12$	97%	43.328 (0.311)	98%	42.331 (0.285)	0%	-	
	$n = 321, l_{\text{max}} = 12, l_{\text{max}}^s = 12$	100%	43.008 (0.222)	100%	43.395 (0.194)	1%	42.918 (-)	
$b = 3000 \ s/mm^2$, SNR = 50	$n = 41, l_{\text{max}} = 6, l_{\text{max}}^s = 12$	100%	43.967 (0.289)	100%	40.474 (0.224)	27%	51.279 (1.063)	
	$n = 91, l_{\text{max}} = 10, l_{\text{max}}^s = 12$	98%	44.951 (0.200)	100%	42.454 (0.147)	33%	45.237 (1.371)	
	$n = 321, l_{\text{max}} = 12, l_{\text{max}}^s = 12$	100%	44.655 (0.172)	100%	44.199 (0.177)	99%	47.415 (0.361)	

Table S2: The performance of three methods (**BJS**, **SCSC**, **SHridge**) for two fibers with separation angle 45°. The mean of estimated separation angle and the standard error with detection rates are reported under 18 different scenarios.

Two Fibers, Separation Angles (60°, 75°, 90°)

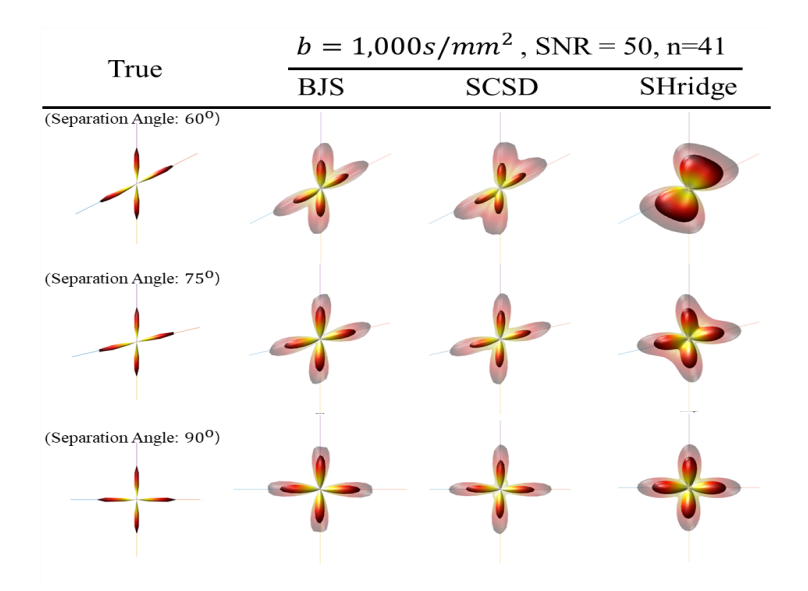


Figure S2: Two fibers with three separation angles (60°, 75°, 90°). The solid lines are the true fiber directions. The opaque part and the semitranslucent part represent the mean estimated FODs across 100 replicates and the mean plus two standard deviations of the estimated FODs.

	$b = 1000s/mm^2$, SNR = 50, $n = 41$, $l_{\text{max}} = 6$, $l_{\text{max}}^s = 12$									
Separation Angle		BJS		SCSD		${ m SHridge}$				
	D.R.	Mean (s.e.)	D.R. Mean (s.e.)		D.R.	Mean (s.e.)				
60	93%	61.235 (0.548)	90%	52.175 (0.810)	43%	65.895 (1.545)				
75	98%	75.086 (0.357)	83%	72.691 (0.319)	77%	80.165 (0.565)				
90	100%	88.175 (0.208)	86%	88.575 (0.175)	93%	86.764 (0.252)				

Table S3: The performance of three methods (**BJS**, **SCSC**, **SHridge**) for two fibers with three separation angles (60°, 75°, 90°). The mean of estimated separation angle and the standard error with detection rates are reported.

Three Fibers, Separation Angles (60°, 90°)

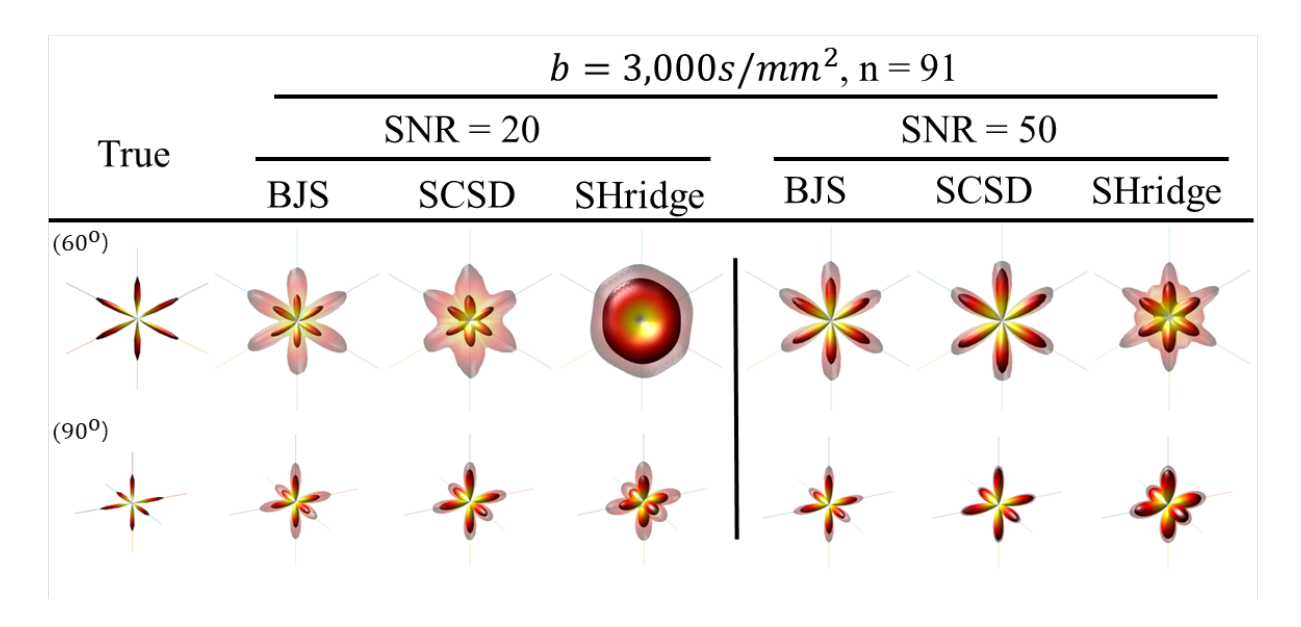


Figure S3: Three fibers with two separation angles (60°, 90°). The solid lines are the true fiber directions. The opaque part and the semitranslucent part represent the mean estimated FODs across 100 replicates and the mean plus two standard deviations of the estimated FODs.

			$b = 3000 s/mm^2, n = 91, l_{\rm max} = 10, l_{\rm max}^s = 12$										
Seperation Angle	SNR	BJS				SCSD				SHridge			
		D.R.	Degree 1	Degree 2	Degree 3	D.R.	Degree 1	Degree 2	Degree 3	D.R.	Degree 1	Degree 2	Degree 3
60	20	73%	59.011	60.769	59.759	38%	58.668	60.806	60.904	0%	-	-	-
60	50	97%	58.963	60.689	60.407	99%	60.341	59.968	59.737	67%	59.510	61.082	60.634
90	20	94%	88.228	87.243	87.527	100%	88.193	87.698	87.724	90%	87.963	87.705	87.378
90	50	98%	89.918	89.699	89.671	100%	89.851	89.671	89.708	100%	89.4114	88.379	87.967

Table S4: The performance of three methods (**BJS**, **SCSC**, **SHridge**) for three fibers with two separation angles (60°, 90°). The mean of estimated separation angle and the standard error with detection rates are reported.

S.3 More details about HCP application

Image Specification

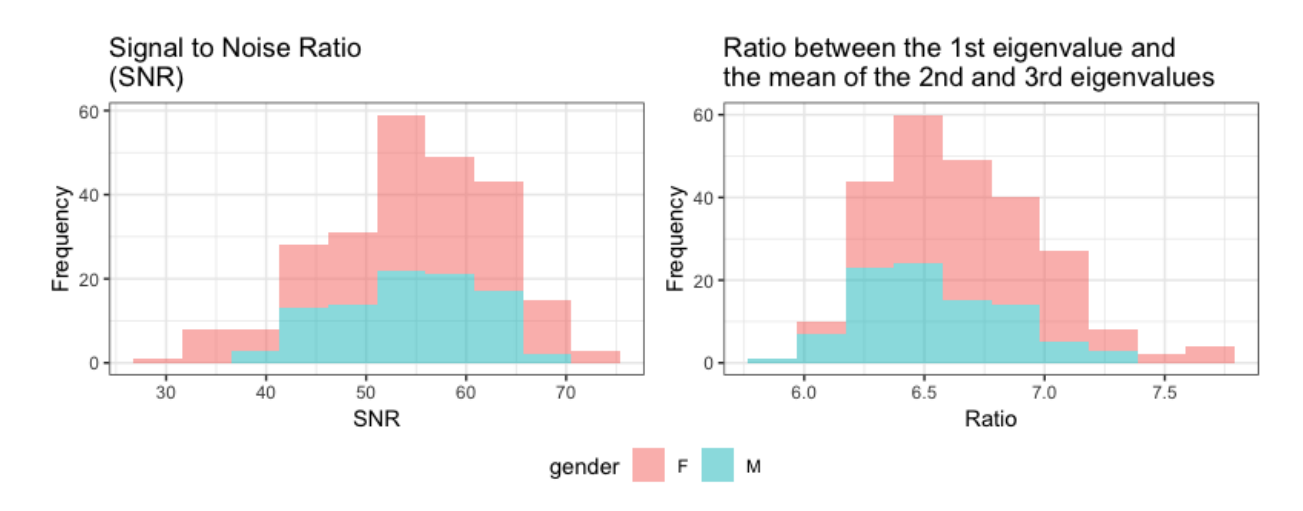


Figure S4: HCP application: Estimated SNR and response function across subjects

Subcortical Location in MNI152 Space

		Left		Right					
Subcortical compartment	NI	MN	I coordir	ates	NI	MNI coordinates			
	Number of Voxel	X	Y	Z	Z Number of Voxel	X	Y	Z	
Accumbens	762	(-18,-2)	(2,24)	(-18,4)	820	(2,20)	(2,24)	(-18,4)	
Amygdala	2083	(-38,-6)	(-20,12)	(-36,-6)	1864	(8,36)	(-22,8)	(-36,-4)	
Caudate	2834	(-24,-2)	(-34,32)	(-12,32)	2740	(2,24)	(-34,32)	(-12,32)	
Hippocampus	3892	(-42,-2)	(-48,2)	(-36,16)	3834	(0,40)	(-48,0)	(-34,16)	
Pallidum	1634	(-32,-8)	(-24,14)	(-14,10)	1584	(8,32)	(-26,12)	(-14,12)	
Putamen	3207	(-38,-8)	(-26,24)	(-18,20)	3168	(8,36)	(-30,24)	(-18,20)	
Thalamus	3760	(-30,2)	(-40,4)	(-10,24)	3693	(-4,30)	(-40,4)	(-10,24)	

Table S5: Subcortical region in template space (MNI152)

Two-way ANOVA with Proportional Volume

Response Variable	Proportional Volume								
Factor	Gender (G)	(G) × (H)							
Accumbens	0.516	0.594	0.639						
Amygdala	0.516	0.594	0.639						
Caudate	0.000	0.913	0.639						
Hippocampus	0.001	0.913	0.671						
Pallidum	0.006	0.594	0.739						
Putamen	0.000	0.594	0.670						
Thalamus	0.000	0.594	0.639						

Table S6: Two-way ANOVA FDR adjusted pvalues: Response – proportional volume of an ROI; Factors – gender, handedness